Supporting Information

The Multifunctionality of Lanthanum-Strontium Cobaltite Nanopowder: High-Pressure Magnetic Studies and Excellent Electrocatalytic Properties for OER

Hanlin Yu[a], Nikita Liedienov[a,b,*], Igor Zatovsky[c], Denys Butenko[d,*], Igor Fesych[e,f], Wei Xu[g], Chunrui Song[h], Quanjun Li[a], Bingbing Liu[a], Aleksey Pashchenko[a,b,f], Georgiy Levchenko[a,b,*]

[a]*State Key Laboratory of Superhard Materials, International Center of Future Science, Jilin University, 130012 Changchun, P.R. China*
[b]*Donetsk Institute for Physics and Engineering named after O.O. Galkin, NASU, 03028 Kyiv, Ukraine*
[c]*F.D. Ovcharenko Institute of Biocolloidal Chemistry, NASU, 03142 Kyiv, Ukraine*
[d]*Department of Physics, Southern University of Science and Technology, Shenzhen 518055, P.R. China*
[e]*Taras Shevchenko National University of Kyiv, 01030 Kyiv, Ukraine*
[f]*Institute of Magnetism NASU and MESU, 03142 Kyiv, Ukraine*
[g]*State Key Laboratory of Inorganic Synthesis and Preparative Chemistry, College of Chemistry, Jilin University, Changchun, 130012, P.R. China*
[h]*Baicheng Normal University, 137099 Baicheng, China*

*Corresponding author
E-mail address: nikita.ledenev.ssp@gmail.com (N.A. Liedienov)
debut98@ukr.net (D.S. Butenko)
g-levch@ukr.net (G.G. Levchenko)

Determination of the size of the coherent scattering region in the $La_{0.6}Sr_{0.4}CoO_3$ nanopowders

The size of the coherent scattering region D_{XRD} was determined using the X-ray line broadening method. The average size D_{XRD} in the $La_{0.6}Sr_{0.4}CoO_3$ (LSCO) nanopowders is related to the dimensional broadening of β for diffraction reflection (012) according to the Scherrer equation [1]:

$$D_{XRD} = K\lambda / \beta\cos\theta, \quad \text{(S1)}$$

where D_{XRD} is the size of scattering crystallites in nm; $\lambda = 0.15406$ nm is the wavelength of X-ray radiation; $K = 0.9$ is a constant that depends on the method for determining the line broadening and crystal shape; β is the width of the intensity distribution curve at half of the height of the maximum of the reflex in radians; θ is the diffraction angle in degrees.

Considering that the integral width of the peak in the diffractogram is approximated by the pseudo-Voigt function with a large (up to 90% or more) contribution of the Lorentz function, the Lorentzian was used to describe the shape of the diffraction reflection at $2\theta \approx 23.2°$ (see Figure S1). In order to exclude the instrumental broadening β_{inst}, standard silicon (Si) X-ray powder diffraction data (JCPDS89-2955) was recorded under the same condition in a separate experiment. The integral width of the peak was calculated by the formula [2]:

$$\beta_{012} = \beta_{exp} - \beta_{inst}, \quad \text{(S2)}$$

where β_{exp} is the experimental width of the sample peak at half the maximum intensity; β_{inst} is an instrumental broadening of the diffraction line, which depends on the design features of the diffractometer (in radians).

The average size of the D_{XRD} was obtained using an approximation of the experimental values of the intensity of the diffraction maximum with a Bragg angle of $2\theta \approx 23.2°$ and considering all the experimental parameters in equation (S1) (see Table S1).

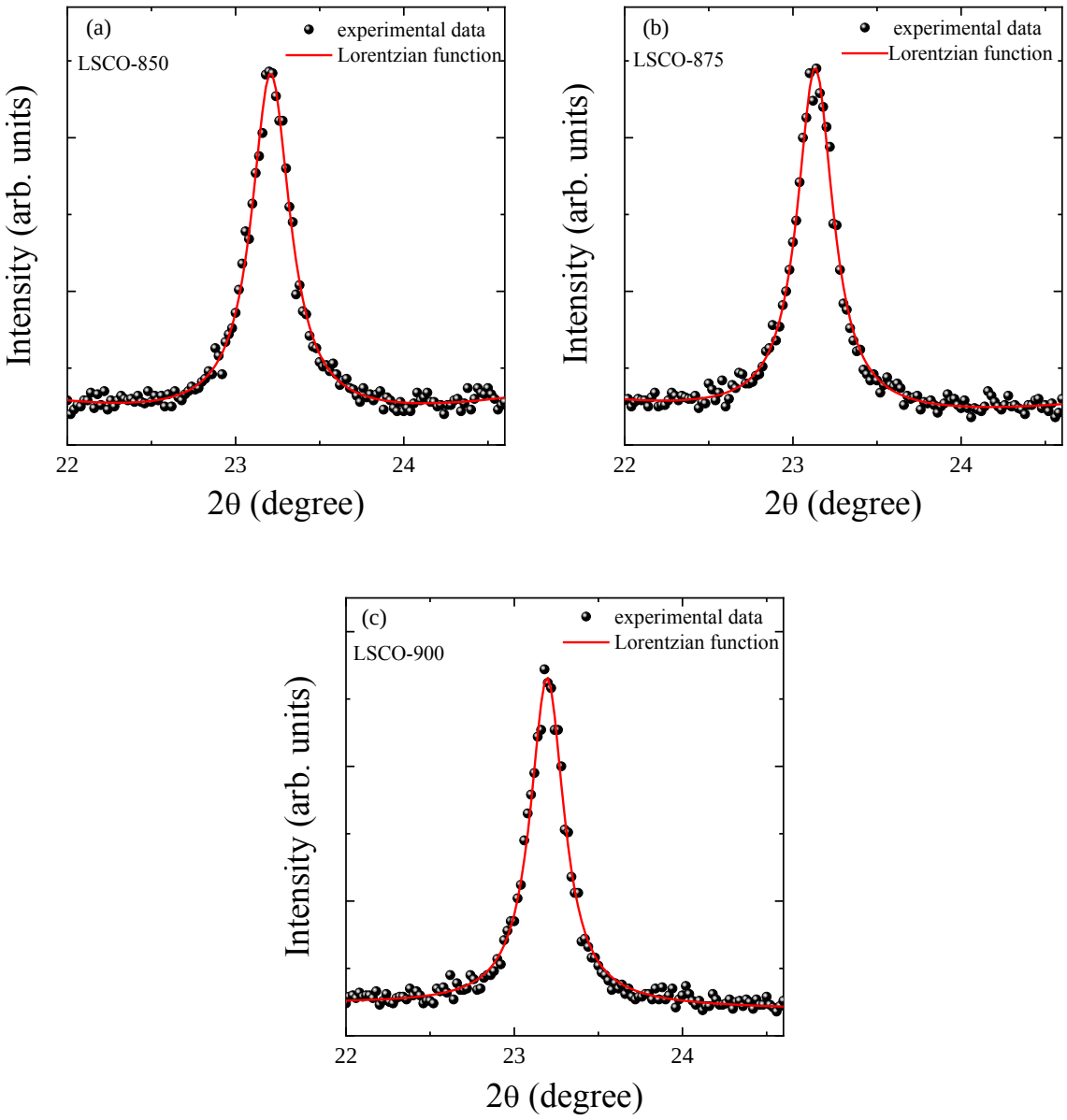

Figure S1. The diffraction patterns and their approximation by Lorentzian function for the LSCO nanopowders in the region of the (012) reflection with an angle of $2\theta \approx 23.2°$.

Table S1

The experimental parameters in Eq. (S1) and the average size of the coherent scattering regions D_{XRD} for the LSCO nanopowders with different annealing temperatures t_{ann}.

t_{ann} (°C)	2θ (degree)	β (radian)	$\cos\theta$	λ (nm)	K	D_{XRD} (nm)
850	23.208	0.0030	0.97956	0.15406	0.9	48±1
875	23.132	0.0026	0.97969	0.15406	0.9	54±1
900	23.195	0.0024	0.97958	0.15406	0.9	60±1

Electrochemical properties of the LSCO nanopowders

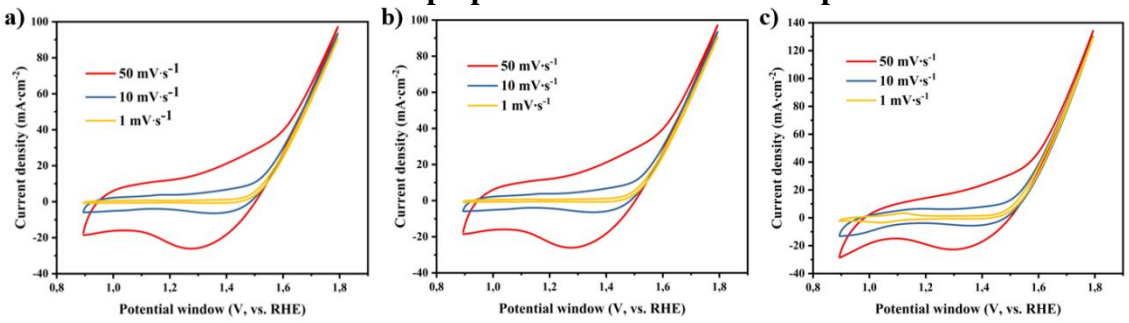

Figure S2. CV curves at different scanning rates for LSCO electrodes: (a) LSCO-850, (b) LSCO-875, (c) LSCO-900.

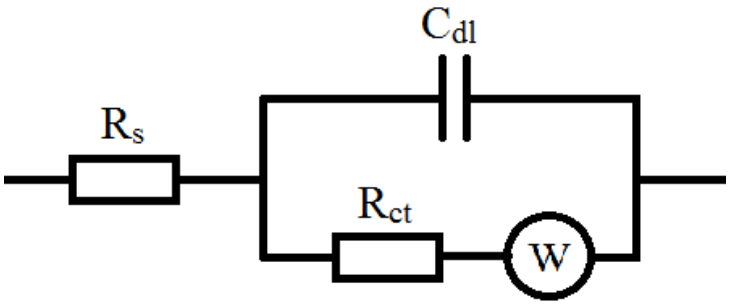

Figure S3. The equivalent scheme for EIS measurement.

Table S2

The corresponding EIS parameters of the LSCO-850, LSCO-875, and LSCO-900.

Sample	R_s (Ohm)	R_{ct} (Ohm)	C_{dl} (mF)	W ($S \cdot sec^{-5}$)
LSCO-850	1.993	0.62	584.39	0.06821
LSCO-875	1.911	0.53	631.60	0.05478
LSCO-900	1.763	0.36	897.61	0.09678

Electrochemically active surface areas (ECSA) of a material with similar composition are proportional to its electrochemical double-layer capacitance (C_{dl}), measured by CV in a non-Faradaic region at different scan rates [3]. Then, the double-layer capacitance (C_{dl}) was estimated by plotting the Δj *vs* RHE as a function of the scan rate (see Figure S4(e-h)):

$$C_{dl} = \frac{d(\Delta j)}{2dV}. \quad (S3)$$

The ECSA can be calculated from the C_{dl} according to the following:

$$ECSA = \frac{\text{specific capacitance of catalyst}}{\text{specific capacitance of carbon fiber per cm}^2}, \quad (S4)$$

where C_s is the specific capacitance of a flat surface with 1 cm^2 of the entire surface area [4].

Calculation values of ECSA for the LSCO samples are the following:

$$\mathrm{ECSA(LSCO\text{-}850)} = \frac{584.39\ \mathrm{mF}}{36.59\ \mathrm{mF}\cdot\mathrm{cm}^{-2}} = 15.97\ \mathrm{cm}^2,$$

$$\mathrm{ECSA(LSCO\text{-}875)} = \frac{631.6\ \mathrm{mF}}{36.59\ \mathrm{mF}\cdot\mathrm{cm}^{-2}} = 17.26\ \mathrm{cm}^2,$$

$$\mathrm{ECSA(LSCO\text{-}900)} = \frac{897.61\ \mathrm{mF}}{36.59\ \mathrm{mF}\cdot\mathrm{cm}^{-2}} = 24.53\ \mathrm{cm}^2.$$

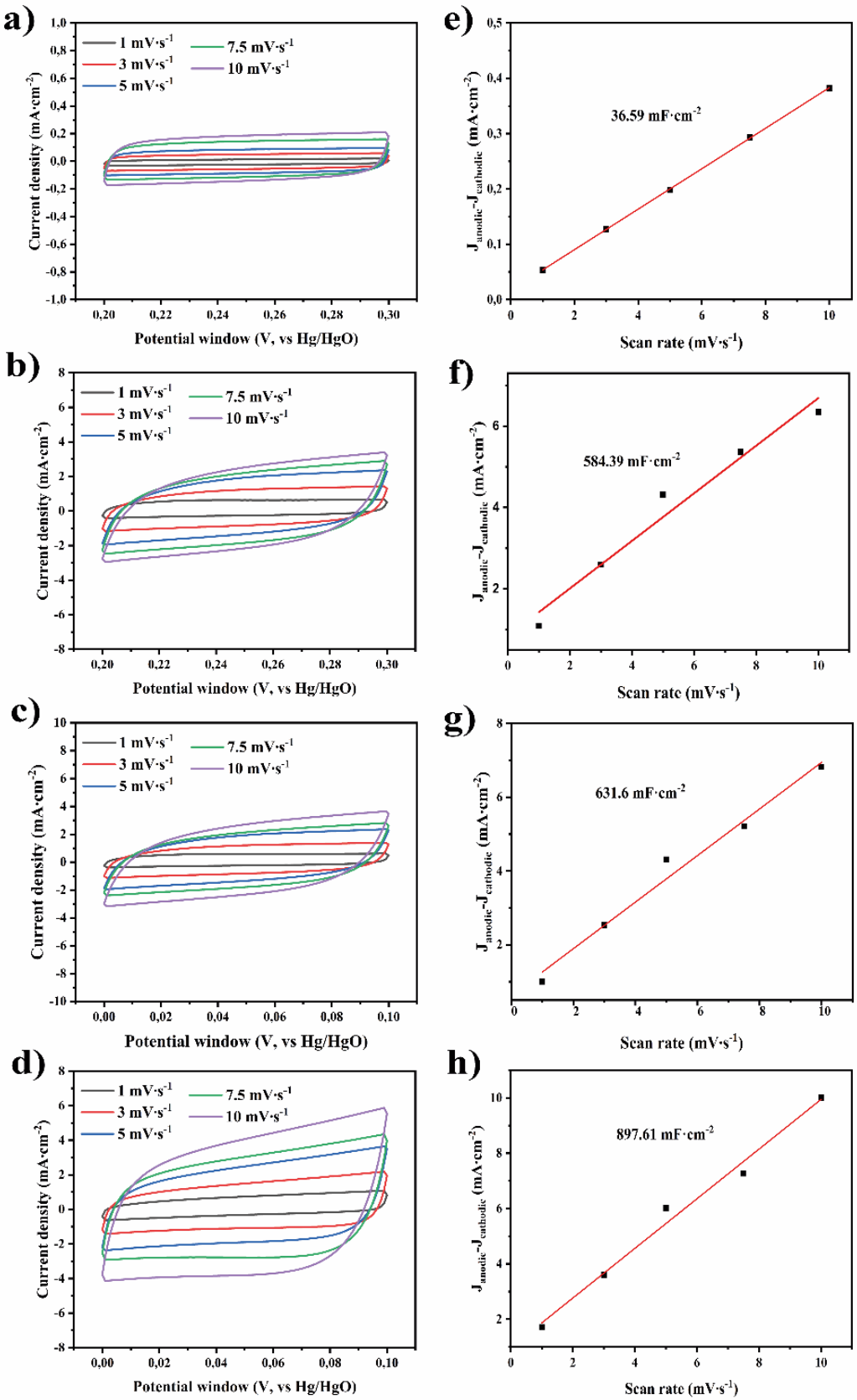

Figure S4. Cyclic voltammograms of (a) LSCO-850, (b) LSCO-875, (c) LSCO-900, and (d) carbon fiber at different scan rates in the voltage range of 0–0.1 V. Δj *versus* RHE as a function of the scan rate for the (e) LSCO-850, (f) LSCO-875, (g) LSCO-900, and (h) carbon fiber.

Table S3

Overpotential OER and Tafel slope values for LSCO samples according to LSV tests.

Sample	Overpotential OER			Tafel slope
	η_{10} (mV)	η_{20} (mV)	η_{100} (mV)	(mV·dec^{-1})
	Initial values			
LSCO-850	285	310	379	74.7
LSCO-875	275	296	360	80.9
LSCO-900	265	290	360	81.7
RuO_2	320	356	534	92.6
After 24 h of incessant electrolysis (current density 10 mA·cm^{-2})				
LSCO-850	362	401	543	121.8
LSCO-875	335	363	444	94.7
LSCO-900	312	338	410	87.7
Change in LSV value after CP test (current density 10 mA·cm^{-2}), %				
LSCO-850	+27.0	+29.4	+43.3	–
LSCO-875	+21.8	+22.6	+23.3	–
LSCO-900	+17.7	+16.6	+13.9	–

For determination of the number of active sites involved in OER based on the redox peak method, we used the following [5,6]:

$$C = \frac{\int \text{area of reduction peak/scan rate}}{\text{Charge of one electron}}, \quad \text{(S5)}$$

where C is the surface concentration of active sites in VA. The area under formation peak for the LSCO-900 = 0.000629 VA (see Figure S5). Therefore, the associated charge is 0.000629 VA / 0.01 V s^{-1} = 0.0629 A s (or) C. Charge of one electron is 1.602·10^{-19} C. So, the surface concentration of active sites is 0.0629 C / 1.602·10^{-19} C = 3.93·10^{17}. The number of active sites was determined similarly for the LSCO-850 and LSCO-875, which were 3.28·10^{17} and 3.64·10^{17}, respectively.

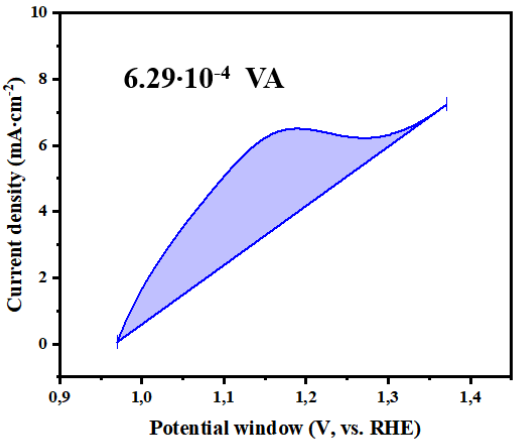

Figure S5. Calculation area under oxidation peak of the LSCO-900.

The turn over frequency (TOF) for the LSCO-900 can be calculated at each different current density value at 1.53–1.58V vs. RHE, and the corresponding expression is given below[5]:

$$TOF = j \cdot \frac{N_A}{n \cdot F \cdot C}, \quad \text{(S6)}$$

where j = Current density (A cm^{-2}); N_A = Avogadro number (6.02214×10^{23} mol^{-1}); F = Faraday's constant (96485 C mol^{-1}); n = Number of electrons transferred for OER n = 4; C = Surface concentration of active sites.

TOF values for the LSCO-900 sample at a potential of 1.53 V and 1.58 V vs. RHE are given by $TOF_{LSCO-900} = [(27.1 \cdot 10^{-3})(6.02214 \cdot 10^{23})] / [(96485)(4)(3.93 \cdot 10^{17})] = 0.11\ s^{-1}$ and $TOF_{LSCO-900} = [(85.03 \cdot 10^{-3})(6.02214 \cdot 10^{23})] / [(96485)(4)(3.93 \cdot 10^{17})] = 0.34\ s^{-1}$, respectively. TOF values for all LSCO samples are plotted in Figure S6.

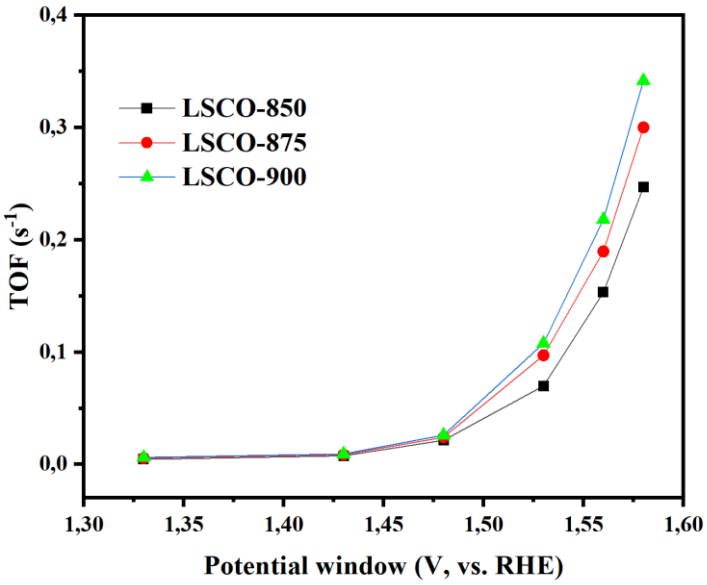

Figure S6. TOF plots of the LSCO samples.

Table S4

The value of overpotential OER during electrolysis for LSCO samples according to the results of the CP tests.

Sample	Electrolysis time (h)				
	0	1	4	12	24
LSCO-850	285	317 (+32)	335 (+50)	346 (+61)	362 (+77)
LSCO-875	275	307 (+32)	320 (+45)	328 (+53)	334 (+64)
LSCO-900	265	288 (+23)	300 (+35)	306 (+41)	312 (+47)

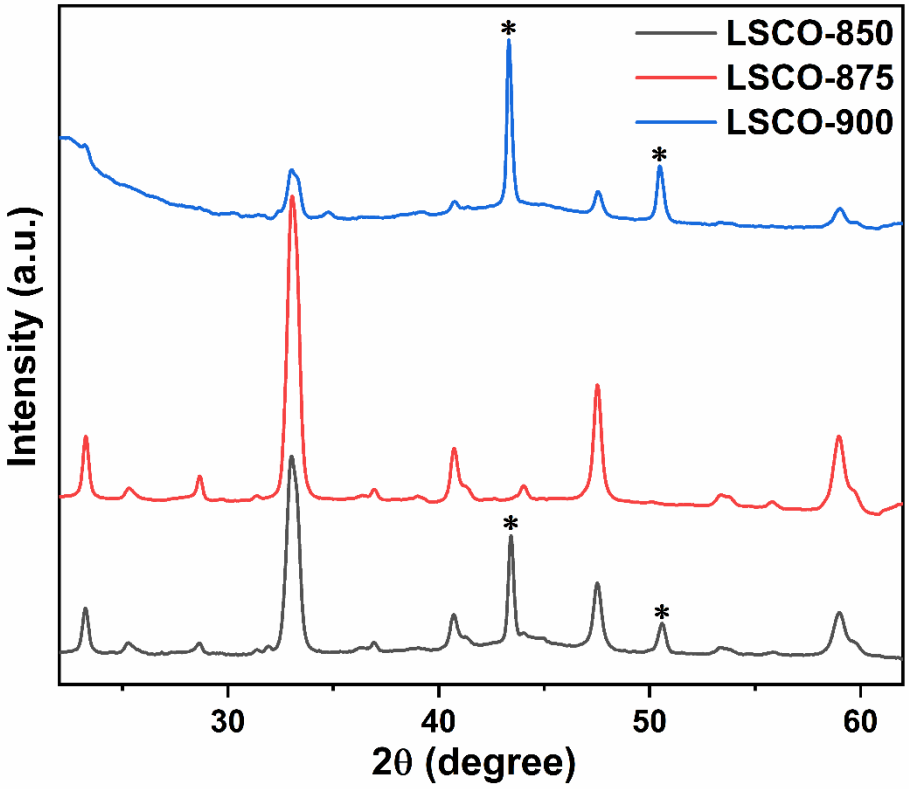

Figure S7. The XRD results for the LSCO electrode after the CP test in 1 M KOH electrolyte (* diffraction reflexes of metallic copper caused by the copper holder of the electrode material).

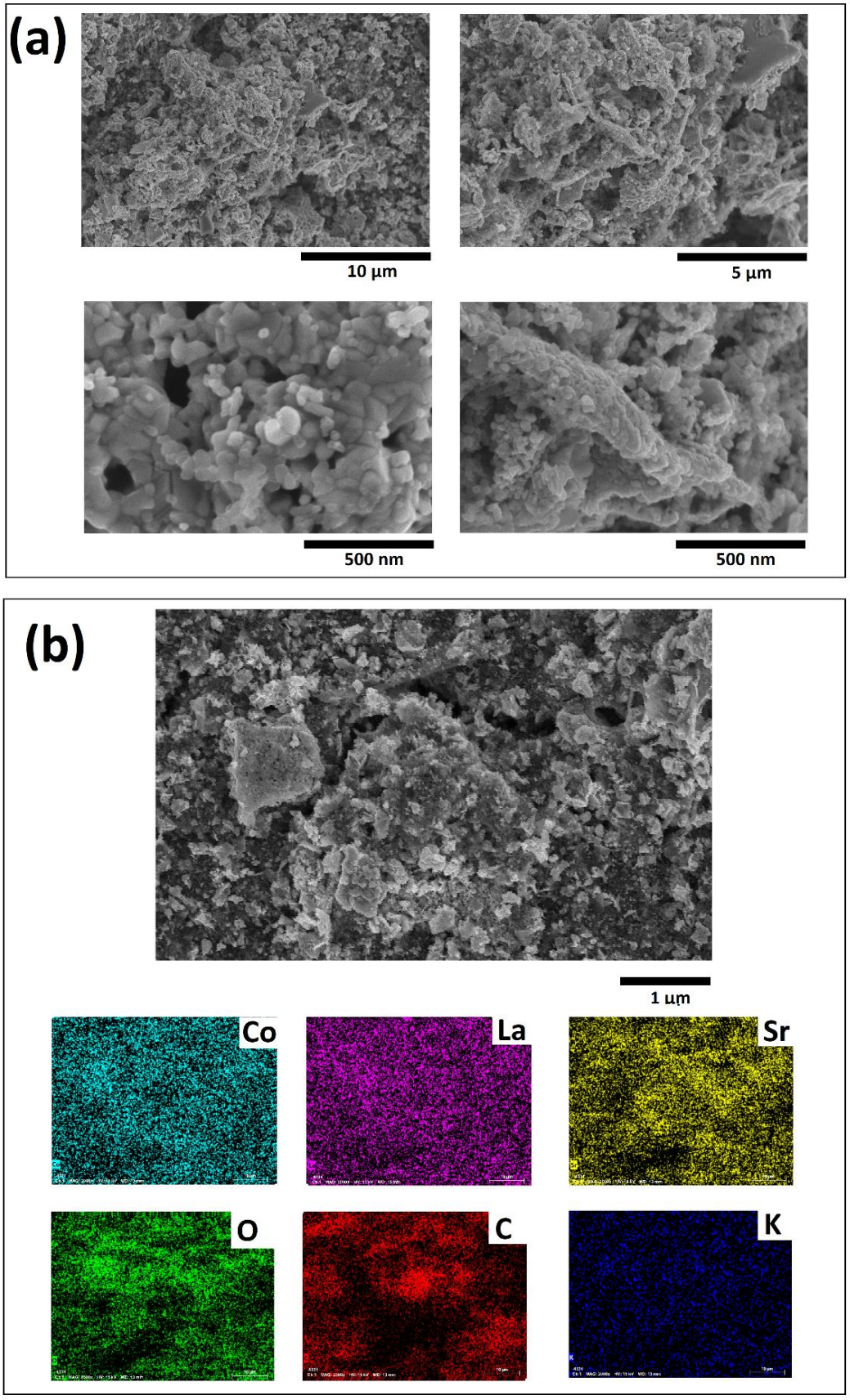

Figure S8. SEM images and mapping of surface elements of the LSCO-850 electrode after long-term electrolysis.

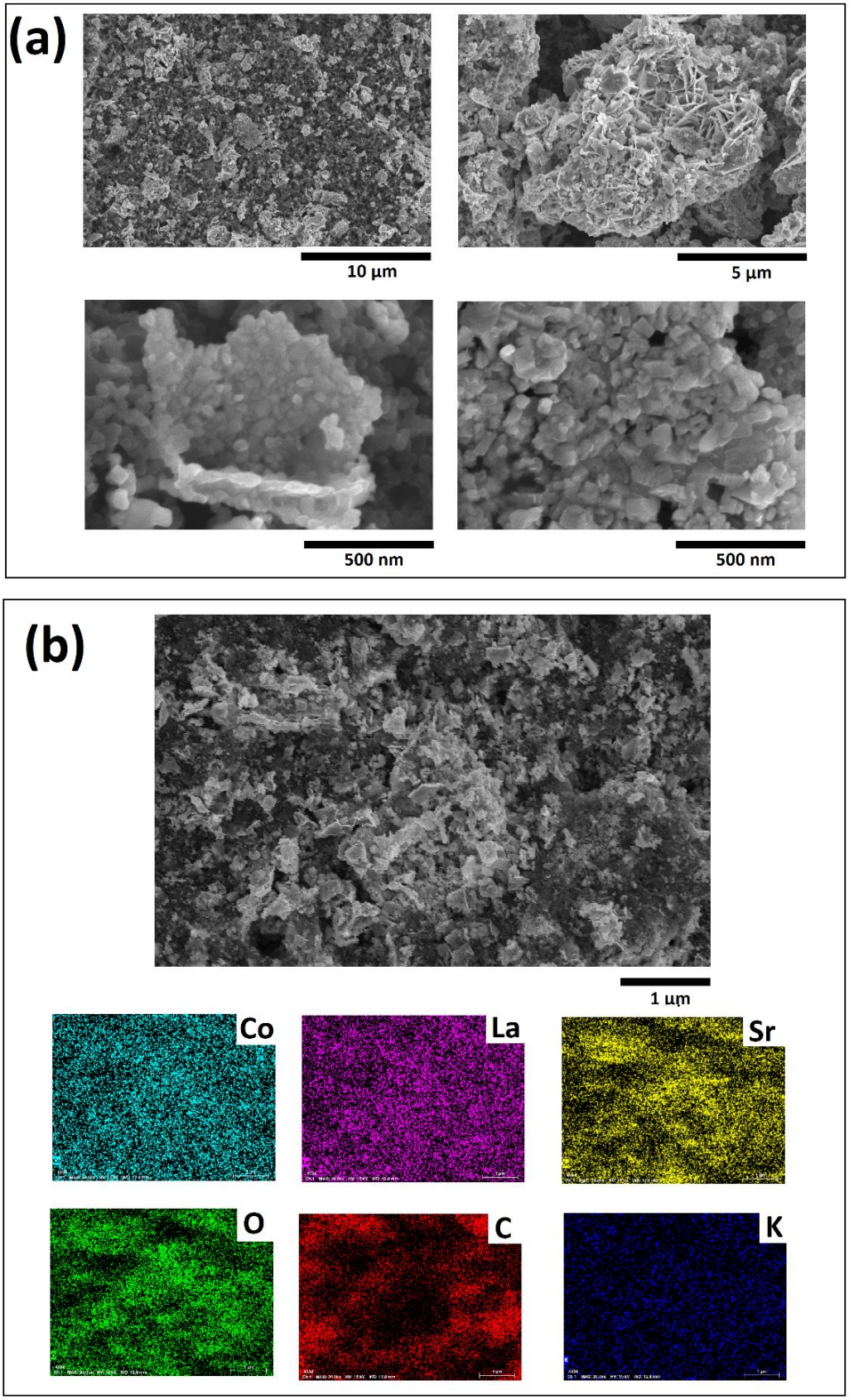

Figure S9. SEM images and mapping of surface elements of the LSCO-875 electrode after long-term electrolysis.

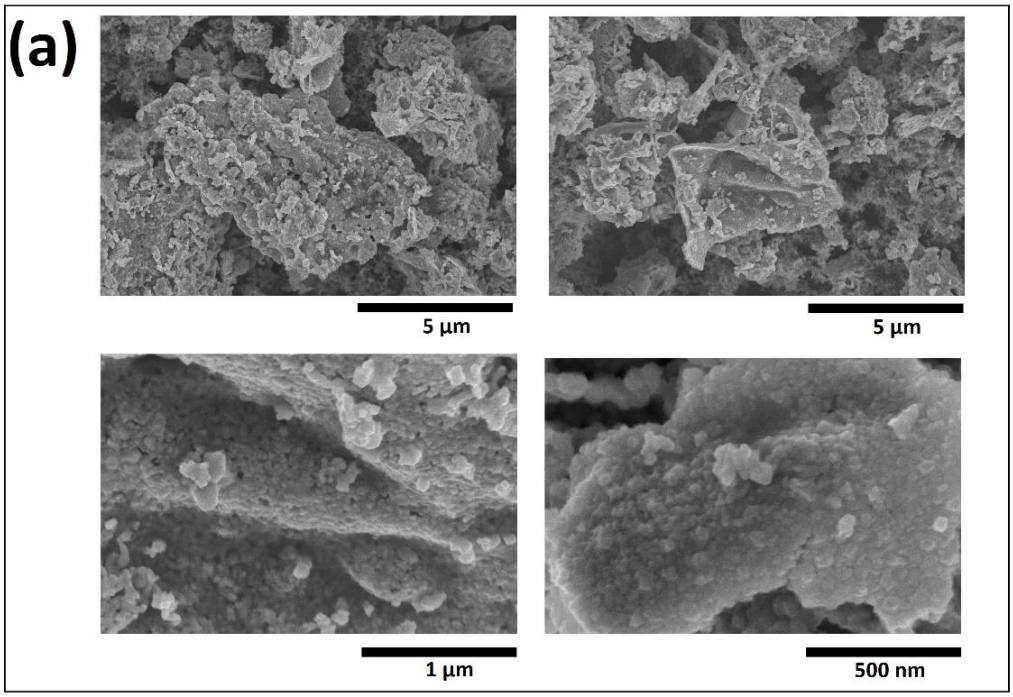

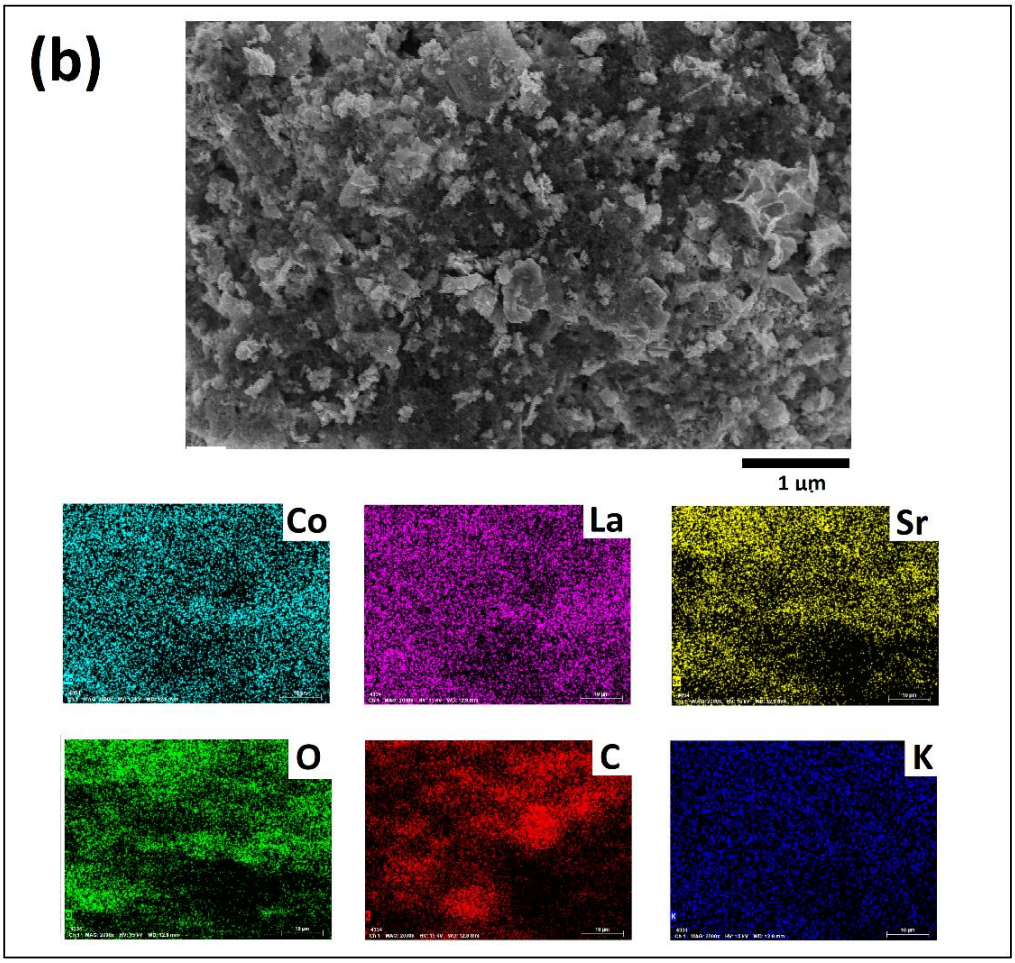

Figure S10. SEM images and mapping of surface elements of the LSCO-900 electrode after long-term electrolysis.

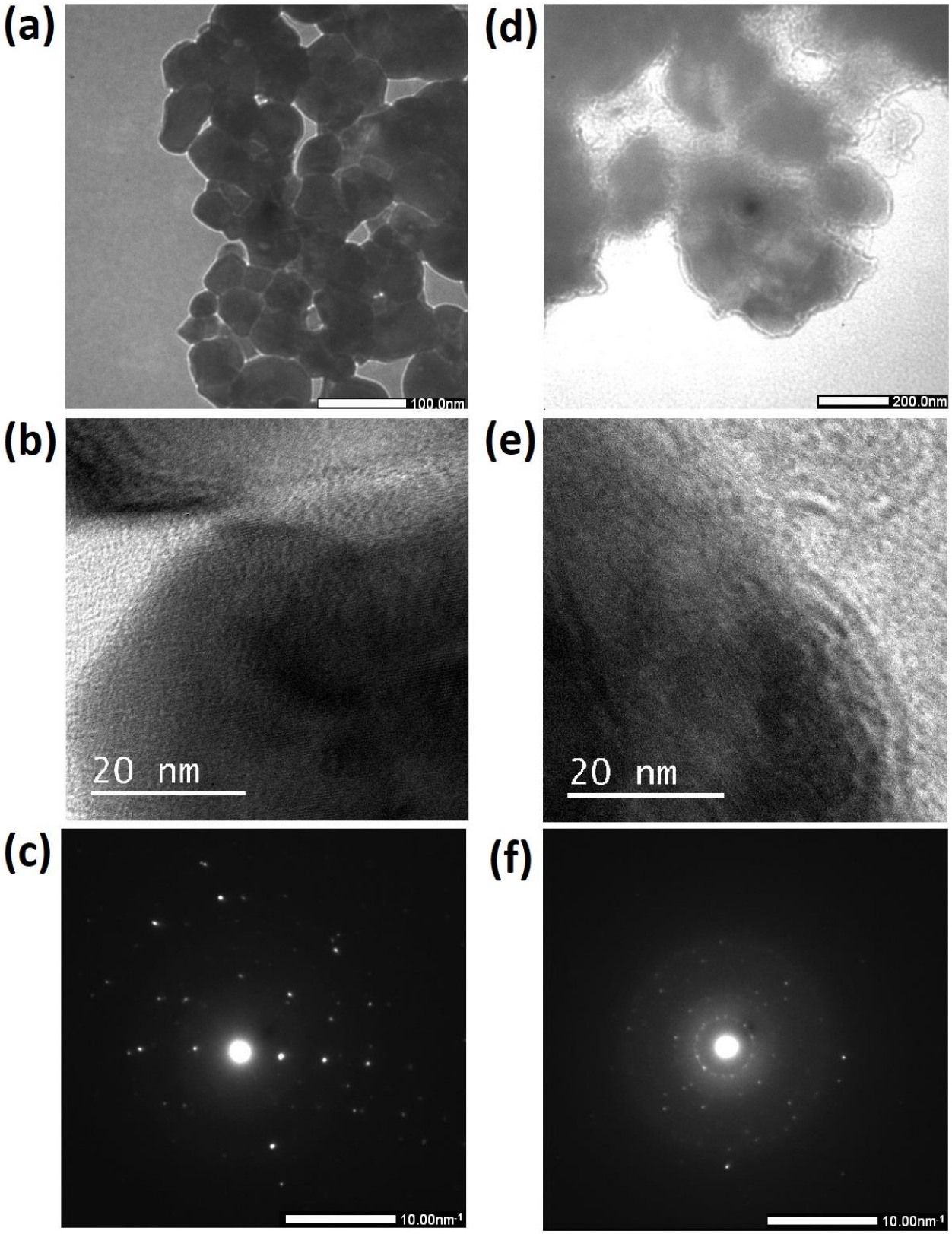

Figure S11. TEM and SAED images of the LSCO-900 electrode before (a-c) and after (d-f) long-term electrolysis.

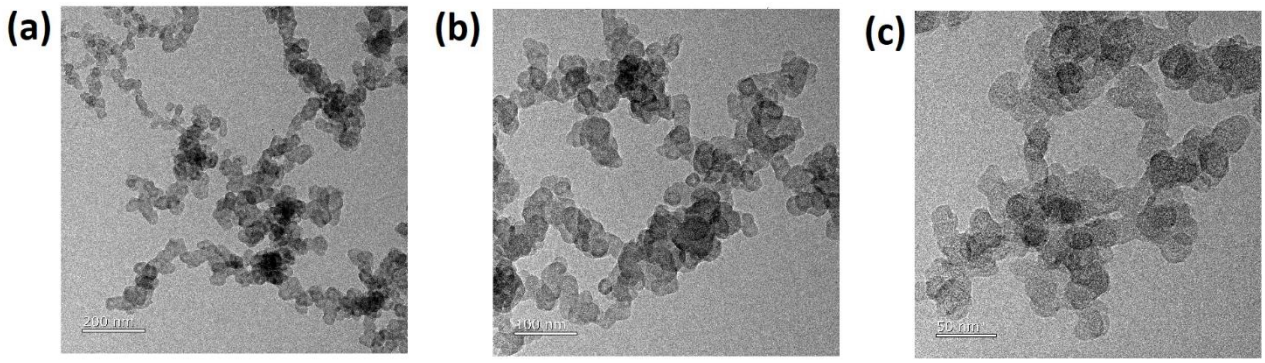

Figure S12. TEM images of the LSCO-900 electrode after long-term electrolysis with a different scale of 200 nm (a), 100 nm (b), and 50 nm (c).

Figures S11 and S12 show TEM and SAED images of the LSCO-900 catalyst before and after long-term electrolysis. Before catalysis, LSCO-900 particles show a clear contour (Figure S11(a)) and HRTEM reveals the presence of interplanar lattice distances on the surface of the particles (Figure S11(b)). In addition, the SAED pattern indicates a crystalline nature of the sample (Figure S11(c)). After long-term electrolysis, an additional layer appears on the surface of the particles (Figure S11(d)). It can also be observed by comparing the additional TEM images shown in Figure S12. The thickness of the amorphous layer formed on the surface of nanoparticles is insignificant, but this layer is observed on HRTEM (Figure S11(e)). SAED rings with broadening and spots are observed in Figure S11(f). Usually, the diffraction ring's expansion occurs when an amorphous layer is formed on the surface (this refers to the interface between the metal and the amorphous oxide coating or the interface between the crystalline oxide and the amorphous phase). In our case, a similar situation exists. Therefore, it can be stated that after catalysis, the surface of the LSCO-900 sample is covered with an amorphous layer. Accordingly, this layer provides excellent catalytic properties.

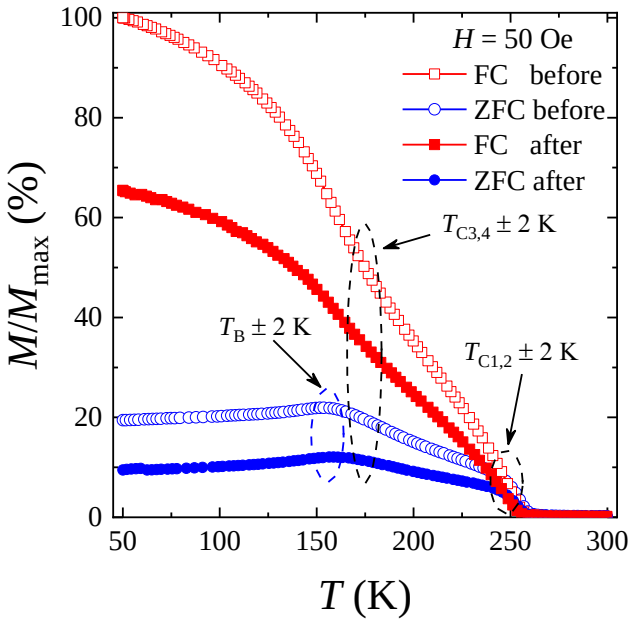

Figure S13. Temperature dependences of the relative magnetization $M/M_{max}(T)$ in the field of H = 50 Oe for the LSCO-900 before and after electrocatalysis in 1M KOH (pH = 14) media at 10 mA·cm^{-2} for 24 h.

Figure S13 shows the temperature dependences of the relative magnetization $M_{ZFC}/M_{max}(T)$ and $M_{FC}/M_{max}(T)$ for the LSCO-900 sample before and after long-term electrolysis in the magnetic field H = 50 Oe. An interesting fact is that the LSCO-900 sample preserves its nanomagnetism even after long-term 24 h electrolysis in 1M KOH (pH = 14) media at 10 mA·cm^{-2}: (i) the Curie temperatures for smaller $T_{C3,4}$ and bigger $T_{C1,2}$ particles are almost the same within the accuracy of the measurements; (ii) there is unchanged blocking temperature $T_B \approx 170$ K, indicating blocked and unblocked states of the nanoparticles below and higher this temperature; (iii) at $T > T_{C1,2}$, all magnetic nanoparticles go into the PM state as well; and (iv) the significant thermo-magnetic irreversibility between the ZFC and FC curves associated with the magnetic frustration is also observed. However, this ZFC-FC gap after long-term electrolysis reduces from 81 to 56% upon 50 K. It makes the magnetic subsystem more homogeneous, probably due to the loss of nanoparticles' "dead" shell (randomly oriented PM and AFM Co^{3+}–O^{2-}–Co^{3+} and Co^{4+}–O^{2-}–Co^{4+} components) [7]. The relative change of magnetization $\Delta M/M_{max}$ also decreases because of the mass loss of the LSCO-900 sample and, as a result, reducing the number of magnetoactive Co ions and/or changing their oxidation states, which may be controlled by the duration and media of the electrolysis [8]. However, it demands

additional and more deep research. Moreover, almost unchanging in Curie temperatures means that the FM Co^{3+}–O^{2-}–Co^{4+} interactions are maintained even after electrolysis. All this indicates the transforming surface and changing ions' coordination surrounding of the LSCO-900 sample after long-term electrolysis.

References

(1) Patterson, A. The Scherrer Formula for X-ray Particle Size Determination. *Physical Review* **1939**, *56* (10), 978.

(2) de Keijser, Th.; Mittemeijer, E. J.; Rozendaal, H. C. F. The Determination of Crystallite-Size and Lattice-Strain Parameters in Conjunction with the Profile-Refinement Method for the Determination of Crystal Structures. *J. Appl. Cryst* **1983**, *16*, 309-316.

(3) Butenko, D. S.; Li, S.; Kotsyubynsky, V. O.; Boychuk, V. M.; Dubinko, V. I.; Kolkovsky, P. I.; Liedienov, N. A.; Klyui, N.; Han, W.; Zatovsky, I. V. Palladium Nanoparticles Embedded in Microporous Carbon as Electrocatalysts for Water Splitting in Alkaline Media. *International Journal of Hydrogen Energy* **2021**, *46* (41), 21462-21474.

(4) Li, J.; Wei, G.; Zhu, Y.; Xi, Y.; Pan, X.; Ji, Y.; Zatovsky, I. V.; Han, W. Hierarchical NiCoP Nanocone Arrays Supported on Ni Foam as an Efficient and Stable Bifunctional Electrocatalyst for Overall Water Splitting. *Journal of Materials Chemistry A* **2017**, *5* (28), 14828-14837.

(5) Anantharaj, S.; Kundu, S. Do the Evaluation Parameters Reflect Intrinsic Activity of Electrocatalysts in Electrochemical Water Splitting? *ACS Energy Letters* **2019**, *4* (6), 1260-1264.

(6) Anantharaj, S.; Noda, S. Dos and Don'ts in Screening Water Splitting Electrocatalysts. *Energy Advances* **2022**, *1* (8), 511-523.

(7) Liedienov, N. A.; Wei, Z.; Kalita, V. M.; Pashchenko, A. V.; Li, Q.; Fesych, I. V.; Turchenko, V. A.; Hou, C.; Wei, X.; Liu, B. Spin-Dependent Magnetism and Superparamagnetic Contribution to the Magnetocaloric Effect of Non-Stoichiometric Manganite Nanoparticles. *Applied Materials Today* **2022**, *26*, 101340.

(8) Gong, Z.; Xu, W.; Liedienov, N.; Butenko, D.; Zatovsky, I.; Gural'skiy, I.; Wei, Z.; Li, Q.; Liu, B.; Batman, Y. A. Expansion of the Multifunctionality in Off-Stoichiometric Manganites using Post-Annealing and High Pressure: Physical and Electrochemical Studies. *Physical Chemistry Chemical Physics* **2022**, *24* (36), 21872-21885.